Doppler-broadening measurements of positronium thermalization in gases

M. Skalsey, J. J. Engbrecht, C. M. Nakamura, R. S. Vallery, and D. W. Gidley
Randall Laboratory of Physics, University of Michigan, Ann Arbor, Michigan 48109
(Received 15 July 2002; published 28 February 2003)

The formation and subsequent thermalization of positronium (Ps) produced at a few eV in gases are investigated using time-resolved Doppler-broadening measurements of the annihilation photons. A static magnetic field quenches the Ps enabling Doppler energy measurements from 25 to 70 ns after the Ps is formed. Varying the gas density permits a significant range of the thermalization process to be observed. Seven different gases are studied, He, Ne, Ar, H_2, N_2, isobutane, and neopentane. A classical elastic scattering model fits all the gas data reasonably well. For each gas, an elastic scattering cross section and an average Ps formation energy are determined from the classical model fit. When comparisons can be made, these cross sections are often significantly smaller than most quantum-mechanical-theory predictions and most previous experimental results obtained using the angular correlation technique. Various systematic tests have been applied to the apparatus and the analysis, reinforcing the discrepancy with previous works.

DOI: 10.1103/PhysRevA.67.022504 PACS number(s): 36.10.Dr

I. INTRODUCTION

The formation of positronium (Ps), the positron-electron (e^+e^-) bound state, can occur in gases as fast e^+ slow down toward thermal energies. In the ground state, Ps is a triplet of spin-one states called ortho-Ps (o-Ps) and a singlet, spin-zero state called para-Ps (p-Ps). In vacuum, o-Ps decays into 3γ with a lifetime of 142 ns ($\lambda_T = 1/\tau = 7.0\ \mu s^{-1}$) and p-Ps decays into 2γ in 125 ps ($\lambda_S = 8.0\ ns^{-1}$). If Ps is formed in gases near atmospheric pressure with a kinetic energy greater than its binding energy of 6.8 eV, collisional dissociation with the gas occurs rapidly [1]. There is a range of low e^+ energies, called the Ore gap [2], where low-energy Ps is formed and lives long enough to be observed to annihilate. With an initial energy of several eV, this Ps will frequently collide with the gas, losing energy and approaching thermal equilibrium with the gas. It is this thermalization process that we wish to study.

Since Ps is neutral, there is no direct Coulomb interaction when scattering with the gas. Assuming that electronic excitations or other inelastic processes are too high in energy to be accessed, only elastic scattering can thermalize Ps. An elastic electron exchange interaction is operative between the e^- in the Ps and one of the e^- from the gas molecule. Also, Ps is strongly polarizable, which together with exchange, results in a relatively strong interaction with most gases. Rigorous calculations of the Ps energy-loss process are extremely complex. In principle, all excited states in Ps and the gas must be included in the calculation, as well as effects only appearing in higher order. Consequently, only the simplest systems are calculated and even then approximations are necessary [3]. Unfortunately, different types of calculations give differing results. Early calculations yielded cross sections that were systematically too large [1], reinforcing the misconception that Ps always thermalizes rapidly in gases.

The direct measurement of Ps-gas cross sections, using a collimated beam of Ps atoms incident on a gas cell, has been done at University College, London [4–7]. Unfortunately, these measurements are unable to access Ps with an energy less than 10 eV, due to problems in forming the collimated Ps beam. The nondissociative thermalization process begins at energies below 10 eV and therefore the London cross sections [4–7] are not directly applicable, except that they sometimes can be compared with the same theoretical calculations of the cross sections.

Previous experiments to directly investigate Ps thermalization in gases have all used the angular correlation of the annihilation radiation (ACAR) technique. In ACAR, two 511-keV photons are examined for the roughly 1-mrad angular deviation from 180°, which measures the transverse momentum of the annihilating system. No time selection for isolating Ps states is presently possible with high-resolution ACAR, although efforts in that direction have recently begun [8]. A further complication is the requirement of small source volumes for high-resolution ACAR. Typical e^+ initial energies are hundreds of keV from radioactive sources, requiring large gas volumes or high pressures to stop the e^+. Two approaches have been taken toward this problem. First, a small gas chamber and very low count rates yielded only qualitative results [9]. Relative measurements between different noble gases at 1-atm pressure showed essentially no differences. A roughly atomic size cross section was inferred for elastic scattering between the Ps and a gas atom [9]. The second approach compared ACAR spectra of silica aerogel in vacuum and then with 1-atm pressure of gas admitted to the aerogel [10,11]. Microvoids in the aerogel are a low quenching region for o-Ps, that is, there are very few collisions between o-Ps and the walls of the microvoids that cause rapid singlet state annihilation. Adding gas to the aerogel, one effectively obtains many small gas chambers for Ps. The Ps is formed in bulk silica, but can thermally diffuse to a surface, from where the Ps is ejected at roughly 0.3 eV into a void [11]. Adding gas to the aerogel, one hopes the silica surface and the bulk remain unchanged so that the Ps ejected into the voids has the same energy distribution in vacuum or with gas. The validity of this assumption and their results will be discussed later.

Our initial results were briefly reported in Ref. [12]. The measurements are done with time-resolved Doppler-

broadening spectroscopy (DBS). Only one of the two 511-keV γ rays is observed in a single high-resolution Ge detector. In almost all applications a larger 511-keV peak width is readily evident compared to a nearby nuclear γ-ray peak, a broadening due in our case to Ps motion. A static magnetic field, usually $B=2.85$ kG quenches some of the long-lived *o*-Ps by mixing $m=0$ states [13]. The magnetic quenching also introduces a 2γ decay component into the *o*-Ps $m=0$ substate. This 2γ component is the basis for time-resolved DBS measurements and, in favorable cases, leads to a dominating component of very narrow width in the Doppler spectrum. The intrinsic resolution of the Ge detector is removed in the analysis. The width of the remaining component is directly related to the *o*-Ps kinetic energy when annihilating.

All measurements are performed using a single, time-delayed window, usually 30–50 ns after Ps is formed, for Doppler analysis. By raising or lowering the gas density, the Ps thermalization process can be observed after more or less collisions, tracing out the energy-loss process. It should be noted that this procedure is independent of any assumed model of Ps thermalization, in distinction with previous ACAR measurements [9–11].

This study began as a systematic investigation of anomalous quenching effects in *o*-Ps decay rate measurements, which used the gases Ne, N_2, isobutane, and neopentane, pure and in mixtures [14–16]. Available information at that time on *o*-Ps thermalization indicated that no significant problems should have been encountered. However, it was clear from the analysis of the *o*-Ps decay rate data that anomalous effects were occurring at early times and low gas densities [14–16]. The thermalization of *o*-Ps was suspected and led to these investigations. Indeed, we have found that the thermalization process proceeds significantly slower than was previously believed. The effect on the *o*-Ps decay rate experiment has been investigated by a gas quenching experiment [17] and by simulations of the decay rate experimental data [18]. Three additional gases, beyond the four used in the gas decay rate experiment, have also been studied. These results are for further comparisons with other experiments and/or theory. Since our previous paper [12], more data have been acquired with some of the gases. Further, a number of trials have been run for some gases with various systematic changes in the static magnetic field and the delayed time window used to observe *o*-Ps decay. Finally, a new analysis that is systematically much more robust [19] than that in our previous work [12] has been applied to all of the gases. Only small changes from our previous values [12] are presented here.

II. CLASSICAL THERMALIZATION CALCULATION

The thermalization of Ps formed in a noble gas has been calculated by Sauder [20] under certain assumptions. Principally, classical elastic scattering between the Ps and the gas atoms is assumed. That is, there is a velocity-independent elastic scattering cross section, σ, interpreted as the classical geometric size of the atoms. Further, isotropic or ''*S*-wave'' scattering in the center-of-mass frame is assumed. If the Ps has a kinetic energy less than 5.1 eV, the lowest Ps excitation energy, then Sauder's description could be fairly accurate, all noble gases require >10 eV for excitation.

Since Ps is light compared to the atom that it strikes, very little energy is lost by Ps in each elastic collision,

$$\frac{\Delta E}{E}\approx\frac{m_{\mathrm{Ps}}}{M}, \tag{1}$$

where m_{Ps} is the Ps mass ($2m_e$) and M is the mass of the struck atom. Values of $\Delta E/E=10^{-4}$ to 10^{-5} indicate that numerous elastic collisions are required to thermalize a Ps atom starting at a few eV. From kinetic theory, the rate of collisions is

$$\lambda_c=n\sigma v_{\mathrm{Ps}}, \tag{2}$$

where n is the gas density, σ is the cross section, and v_{Ps} is the Ps speed. Note, the gas atom motion can be ignored since Ps is so light in comparison. Even when thermalized, Ps is moving much faster than the gas atoms.

Sauder's classical elastic scattering theory of Ps thermalization results in a concise expression for the rms average kinetic energy $E(t)$ as Ps asymptotically approaches thermal energy, $E_{th}=\frac{3}{2}kT$ [10,20]:

$$\frac{E}{E_{th}}=\coth^2[\beta+\Gamma nt], \tag{3a}$$

where β is related to the formation energy (E_0) of Ps that can eventually thermalize,

$$\frac{E_0}{E_{th}}=\coth^2[\beta]. \tag{3b}$$

Γ is the rate of thermalization normalized to n, the gas density. This type of gas density dependence for energy moderation will be shown to be a general feature of any model of Ps thermalization, classical or otherwise. (The essential quantity is the number of collisions that Ps has undergone since formation.) The density-normalized thermalization rate, Γ, in Sauder's model is

$$\Gamma=\frac{m_{\mathrm{Ps}}M\sigma}{(m_{\mathrm{Ps}}+M)^2}\langle v_{\mathrm{Ps}}\rangle_{th}\cong\frac{\sigma}{M}p_{th}, \tag{4}$$

where p_{th} is the momentum of thermalized Ps. Maxwell-Boltzmann distributions are used in the rms averaging, implying a fairly broad distribution of energies occurs at any given time after Ps formation.

Using Eq. (3a), the approach of Ps toward thermal equilibrium with the gas at density n can be characterized by the thermalization time: $\tau=1/\Gamma n$. The functional dependence shown in Eq. (3a) implies an extremely rapid approach to the thermal asymptote. Even from an infinite starting energy ($\beta\rightarrow 0$), Ps has slowed to within 70%, 8%, and 1% of E_{th} in times τ, 2τ, and 3τ, respectively.

Inverting Eq. (3a) suggests a method to determine Ps thermalization rates,

$$\operatorname{arccoth}\sqrt{\frac{E}{E_{th}}}=\beta+\Gamma nt. \tag{5}$$

Experimentally, we measure E while varying the product (nt). If Sauder's model is correct, plotting the energy as in Eq. (5) versus (nt) should result in a straight line with slope Γ and intercept β. In this manner, the model can be tested and, if correct, the thermalization rate and the initial energy are thereby determined.

III. QUANTUM-MECHANICAL THERMALIZATION CALCULATIONS

Sauder's classical theory has two main assumptions, a constant cross section for energy loss, σ, and only S-wave scattering. Admitting higher than $L=0$ partial waves complicates the quantum-mechanical description of the thermalization process. The very low Ps energies encountered in this investigation, ~ 1 eV, indicates the dominance of the S-wave component of the scattering amplitude. On the other hand, Sauder's energy independent constant-cross-section assumption must be seriously addressed, by quantum mechanically accounting for all pertinent physical processes occurring during the scattering. In general, the appropriate cross section to describe thermalization is the momentum-transfer cross section σ_m, sometimes called the diffusion cross section [10,21],

$$\sigma_m=2\pi\int_0^{\pi}(1-\cos\theta)\frac{d\sigma}{d\Omega}\sin\theta d\theta, \tag{6}$$

where $d\sigma/d\Omega$ is the elastic differential cross section. The momentum-transfer cross section differs from the total elastic cross section by the factor of $(1-\cos\theta)$ in Eq. (6).

In 1954 Massey and Mohr first considered the slowing down of Ps by inelastic and elastic collisions with atomic hydrogen gas [1]. Once thermalizing Ps is below the energy threshold for electronic excitations, the inelastic channel turns off. The effect of elastic electron exchange during collisions was estimated by Massey and Mohr using the Born-Oppenheimer and other approximations, resulting in a cross section of 22 Å^2 at 6.7 eV, increasing to 200 Å^2 in the zero velocity limit [1]. The consequences from the polarizability of Ps were deemed negligible compared to electron exchange, except at the very lowest energies. Massey and Mohr also point out, in analogy with electron-scattering calculations, that these Ps cross sections are probably overestimates by an amount that increases as the energy decreases [1].

A number of subsequent calculations of Ps scattering from atomic hydrogen, H, have been published. Exact calculations using the first Born approximation have recently appeared [22]. Initially, a static exchange approximation was applied to this problem [23–26]. More sophisticated, closed-coupling calculations, using a three-state approximation [27,28] and an extensive 22 coupled pseudostate formalism [29], are the present state of the art. The most recent results [29], for comparison with Ref. [1], are 9 Å^2 at 6.7 eV and 34 Å^2 at 0 eV.

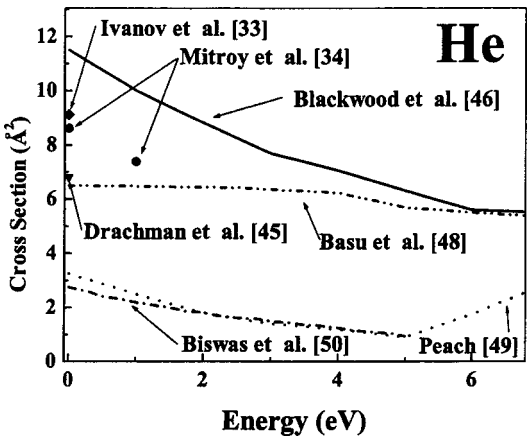

FIG. 1. Elastic cross sections for Ps-He scattering: theory. The total elastic scattering cross section for He, as calculated by theories that include the electron exchange interaction, is shown as a function of the Ps energy.

Calculations of the Ps-H scattering lengths have historically also been of interest since the scattering lengths are related to the zero energy cross section. Reasonable agreement had been obtained in the 1970s between two independent calculations of the scattering lengths [30–32]. The derived cross sections at zero energy are 40 Å^2 [31,32] and 50 Å^2 [30]. More modern versions of these scattering length calculations have obtained cross sections in the range of 30 to 40 Å^2 [33–35]. While it is difficult to assign a theoretical error bar(s) to the preceding calculations, probably $\pm 25\%$ is a reasonable estimate for Ps-H results. Numerous other theoretical papers have been published on Ps scattering from atomic hydrogen focusing on various tests of techniques and other issues [36–40]. The first experimental step toward this difficult problem has been the formation of Ps in atomic hydrogen [41]. Verification of the preceding Ps-H cross-section calculations remains for the future.

Two electron systems, He and H_2 gases, are experimentally much easier to use for Ps formation. Theoretical cross-section calculations in the several eV range are numerous for Ps-He, but only three Ps-H_2 analyses have been carried out [42–44]. The more recent Ps-H_2 cross-section calculations obtain 3 Å^2 in the zero velocity limit and 0.7 Å^2 at 5 eV [43,44]. The three-state coupled-channel analysis [43,44] yielded much smaller cross sections than the older static exchange calculation [42], 170 Å^2 at 0 eV and 11 Å^2 at 5 eV. The most recent Ps-H_2 calculation [44] differs Ref. [43] only at higher energies due to an improved treatment of ionization processes. Using the most recent H and H_2 calculations as a guide, the Ps cross section decreases by a factor of roughly three or four going from zero energy to 5 eV, a very strong dependence compared to the constant-cross-section assumption in Ref. [20].

Most of the Ps-He cross-section calculations predict a softer slope at low energy compared to the H and H_2 results. In Fig. 1 the calculations of the energy dependence of the Ps-He total elastic cross section that include the electron exchange interaction are shown. It is believed to be essential for accurate low-energy calculations to include the effects of

electron exchange during collisions [1,22]. Two scattering length calculations [33,45] are also shown in Fig. 1. Nevertheless, there is significant disagreement (about a factor of 7 at 5 eV) between different Ps-He calculations, but the slow drop off of the cross section with increasing energy is evident for each curve. The difference between total elastic and momentum transfer cross sections, σ_m being the quantity that we measure, will be addressed later. The calculations of Ps-He strongly disagree at energies below 10 eV both in shape and magnitude of the cross section. The calculated zero-energy cross sections are 11.6 Å^2 [46], 9.1 Å^2 [33], 8.6 Å^2 [34], 6.8 Å^2 [45], 6.5 Å^2 [47,48], 3.3 Å^2 [49], and 2.7 Å^2 [50], differing by over a factor of 4. All calculations predict a decreasing cross section with increasing energy, up to 5 eV, but the slope at 1 eV is understandably three times larger in Ref. [46] compared to Ref. [50].

There are two theoretical calculations of the Ps-Ne cross sections versus energy [50,51] and one calculation of the scattering length [34], giving the zero energy cross section. The agreement between calculations is not good, with zero energy cross sections of 7.0 Å^2 [50], 14 Å^2 [51], and 8.4 Å^2 [34] differing by a factor of 2. The situation for Ps-Ar cross sections is similarly discrepant [34,50,51]. The zero energy Ar cross sections are 9.6 Å^2 [50], 28 Å^2 [51], and 11.3 Å^2 [34], differing by a factor of 3. An overall universal disagreement exists for all cases of Ps-atom scattering calculations except H, indicating the difficult problems introduced to elastic-scattering calculations with both projectile and target having internal structure. The heavier noble gases, Kr and Xe, are calculated only in Ref. [51], but we have no data to compare with this calculation. To our knowledge, there are no calculations for molecular targets other than H_2.

A classical elastic scattering theory would seem to be inadequate to describe the interaction of few eV Ps with molecules. Unlike noble gases, molecules may have inelastic electronic excitations that are energetically accessible during Ps thermalization. In addition, there is a fine structure of molecular vibrational excitations superimposed on the electronic excitations and the ground state. For both H_2 and N_2, the low-lying density of vibrational excitations is several levels per eV [52]. Furthermore, a hyperfine structure of rotational molecular excitations dresses all of the above-described levels. The scattering of Ps from a molecule must include, in principle, contributions from these many possible inelastic excitations, as well as the elastic-scattering component.

Inelastic collisions will quickly remove energy from Ps, causing very rapid thermalization compared to the small energy losses [Eq. (1)] in elastic scattering. Even though inelastic cross sections are, in general, much smaller than elastic cross sections, inelastic cross sections could dominate some parts of the thermalization process in molecules. A pertinent example is found in Ref. [42]. The first vibrational level in H_2 is 0.5 eV above the ground state. For Ps energies just above this threshold, the efficiency for inelastic collisions to remove energy (product of energy loss and cross section) is about equal to that for elastic collisions. Clearly, any account of Ps thermalizing in molecular gases must address the issue of numerous possible inelastic channels for energy loss.

While Massey and Mohr outlined these Ps scattering problems almost 50 years ago [1], limited theoretical progress occurred in succeeding decades. Recently, increased interest has been sparked by the gas ACAR results [9–11] and this experiment [12] with low-energy cross sections and at higher energies (10–100 eV) using a Ps beam to obtain total cross section measurements [4–7].

IV. EXPERIMENTAL APPARATUS AND TECHNIQUE

High-resolution Ge γ-ray detectors enable DBS of Ps for this experiment. The Doppler broadening of the 511-keV peak in γ-ray energy spectra is due to a center-of-mass motion (longitudinal component) with the respect to the laboratory at the instant of a 2γ annihilation. Application of time-resolved DBS to investigate *o*-Ps thermalization was first done by Chang *et al.* [53] in an evacuated SiO_2 aerogel. This technique utilizes a magnetic field to perturb and admix the two $m_s=0$ states, mixing *p*-Ps and one of the three *o*-Ps states into two new states, perturbed *p*-Ps and perturbed *o*-Ps [13]. The $m_s=\pm 1$ *o*-Ps states are not affected by the field. Each perturbed state is characterized by the field-free state plus some of the other $m_s=0$ state mixed in. For perturbed *p*-Ps, a small mixture of *o*-Ps hardly makes any difference to our observations. On the other hand, perturbed *o*-Ps is strongly affected by very limited amounts of *p*-Ps being mixed in. For example, the vacuum decay rate of perturbed *o*-Ps, λ', can be significantly quenched with ordinary laboratory fields [13]:

$$\lambda' = \frac{1}{1+y^2}[\lambda_T + y^2\lambda_S], \tag{7a}$$

where

$$y = \frac{x}{1+\sqrt{1+x^2}} \tag{7b}$$

and

$$x = \frac{2g'\mu_B B}{\Delta E_{\mathrm{hfs}}} \cong \frac{B}{36.5\ \mathrm{kG}}. \tag{7c}$$

Typically, $B=2.85$ kG is used for the gas thermalization measurements. At this field, the perturbed *o*-Ps lifetime is reduced to 52 ns from 142 ns at $B=0$. Since this perturbed state has some *p*-Ps mixed in, the usual *o*-Ps 3γ decay is accompanied by some 2γ decays: 64% of the decays are 2γ events at $B=2.85$ kG. This time-delayed 2γ component is used for the DBS measurements of Ps thermalizing in low-density gases.

The Doppler-broadened γ rays have their energy measured with a single Ge detector, crystal size 63 mm$\times$56 mm. The Ge detector resolution is 1.20 keV (full width at half maximum, FWHM) at 511 keV. Throughout this experiment, the instrumental resolution of the Ge detector is monitored on a daily basis using 662-keV γ rays from ^{137}Cs. On a roughly monthly basis, a day-long calibration run is obtained with only a ^{106}Ru source. The ^{106}Ru

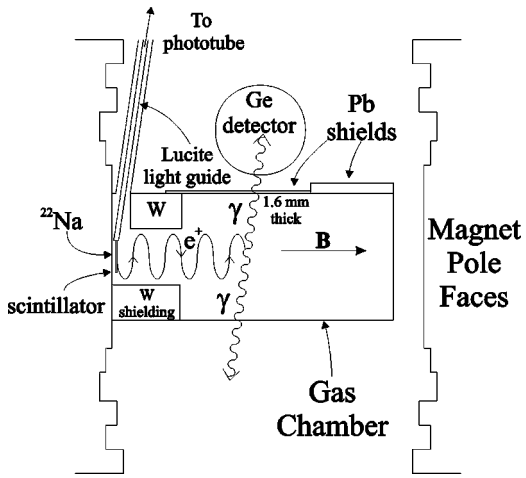

FIG. 2. Experimental apparatus. Positrons from ^{22}Na decay pass through a thin scintillator and enter a gas chamber. A magnetic field confines the trajectories near the axis. Positrons that stop in the gas can form Ps. Annihilation γ rays are detected in a Ge crystal.

decay chain includes a $\approx 19\%$, 511.86-keV γ ray. The instrumental resolution observed in the Ge detector for this nuclear line approximates to better than 10^{-3} that for *o*-Ps.

The experimental apparatus is shown in Fig. 2. The magnet and gas chamber used in this experiment are essentially identical to the apparatus of Refs. [14–16]. As shown in Fig. 2, the Ge detector is situated above the gas chamber, replacing the large volume plastic scintillator detectors used in Refs. [14–16]. Positrons emitted from a 2 μCi ^{22}Na source must pass through a thin plastic scintillator (0.13 mm) before entering the gas. The thin plastic signal is used to start a timing system. The timing of this signal is taken to coincide with Ps formation since positrons thermalize rapidly. The magnetic field confines the positron trajectories to near the chamber axis where some stop and form Ps. A positron beam dump is at the opposite end of the gas chamber from the source region. Lead and tungsten shields are used at both ends of the gas chamber to prevent the Ge detector from directly viewing the source or the beam dump areas.

A turbo-molecular pump is used to evacuate the gas chamber. Fresh gas samples are installed weekly with pressure rises of less than 0.2 Torr/week when sealed. Pressures are measured with a capacitance baratron.

With a lifetime of 52 ns, the magnetically perturbed events can be separated from prompt, short-lived events, *p*-Ps and direct e^+e^- annihilation ($\tau < 1$ ns). This separation requires sufficiently good time resolution of the events. The Ge detector supplies two identical outputs; the first is used for energy, the second for timing. The first goes directly to a spectroscopy amplifier with 6-μs integration. The second timing output is amplified by $\times 100$ with 100-ns differentiation and 100-ns integration. Constant fraction timing discriminators are used for both this amplified and shaped Ge signal and the thin plastic scintillator signal from a coupled photomultiplier tube. Timing discriminator signals are routed to a time to amplitude converter. A time resolution of 13-ns FWHM is obtained for prompt coincidences from this system.

A delayed time window, typically 30 to 50 ns after prompt events, is used to select mainly perturbed *o*-Ps events with $\tau = 52$ ns. This window is essentially free of all prompt events at about the 10^{-3} to 10^{-4} level. Unperturbed *o*-Ps decays from the $m = \pm 1$ substates are present in this delayed time window since their lifetime is near 140 ns. To get 2γ events from unperturbed *o*-Ps, it must be quenched during a gas atom collision. That is, annihilation occurs from the $\vec{S} = 0$ state when the positron in *o*-Ps overlaps with an atomic electron of the opposite spin. This type of collisional quenching is called pick off and it affects each of the gases studied here, as well as the perturbed *o*-Ps component [54].

Another important mechanism to get 2γ events into the delayed time window involves ''slow positrons'' that have fallen below the Öre gap [2] and have lost too much energy to form Ps. These slow positrons thermalize in the gas, diffusing and eventually directly annihilating to 2γ. Slow positrons can live for a long time in gases at low densities, the number of slow positrons and their lifetime is also strongly gas dependent [55].

The final contribution to events in the delayed time window is accidental, uncorrelated coincidences, i.e., random background. Accidental coincidences are essentially an average of all events, regardless of their timing. Because of the small solid angle of the Ge detector for viewing Ps decay γ rays, the accidental background is a significant component of the delayed window events.

With so many possible contributors to the delayed time window, there is concern for systematics disturbing the measurements. Additional delayed time windows, both earlier and later than the usual 30 to 50 ns, are employed in tests to understand and quantify systematic effects. Variations in the magnetic field, both higher and lower than the usual $B = 2.85$ kG, are also employed in the tests.

As normally operated, a logic signal is generated indicating that an event is in the delayed time window. This signal is used as a gating trigger for obtaining DBS data from the energy signal. An 8192 channel energy spectrum is acquired, but only 400 channels centered on 511 keV are actually analyzed. Typical total singles counting rates are 25 kHz in the plastic scintillator positron detector and 800 Hz in the Ge γ-ray energy spectrum. Typical coincidence rates for the delayed timing window trigger are 1 Hz and 0.3 Hz into the actual 511-keV peak in the DBS spectrum. Data are acquired for at least one day at a particular gas density to obtain sufficient statistics for meaningful fits to our DBS model.

V. DBS DATA AND ANALYSIS

A time-resolved DBS spectrum is shown in Fig. 3 for 100-Torr neopentane along with a fit to a model described below. The prominent narrow peak at 511 keV is the signal for this experiment due to perturbed *o*-Ps. The Doppler width of this peak yields the longitudinal component of the *o*-Ps velocity which then gives the *o*-Ps energy. Also centered at 511 keV, a second wider peak of reduced amplitude is shown in Fig. 3. The origins of this wider peak are the background processes contributing to the delayed time window, aside from perturbed *o*-Ps. The wide peak processes are (1) pick

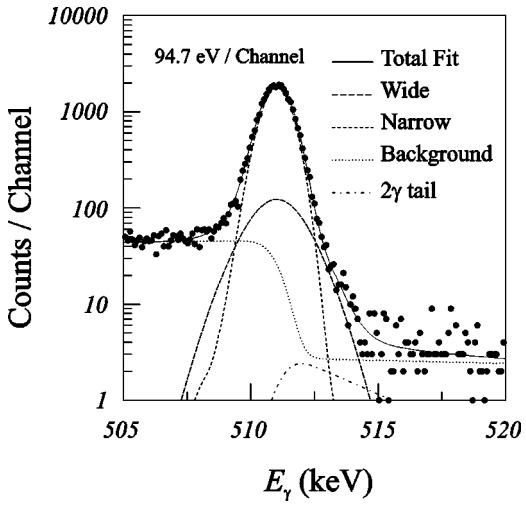

FIG. 3. Typical thermalization data. The Doppler-broadened 511-keV photopeak is resolved into two Gaussians, a step background, and a 2γ tail. The first three components are shown convoluted with the intrinsic detector resolution; the 2γ tail is also convoluted with the narrow Gaussian.

off from *o*-Ps, perturbed and unperturbed; (2) slow positrons; and (3) random accidentals. The amplitude and width of the wide peak are observed to depend on the gas composition and density.

Away from the peaks in Fig. 3, an asymmetric background is observed. The background on the right (higher energy) is due, in part, to accidental coincidences from high-energy γ rays that Compton scatter in the Ge detector with only partial energy deposition. Another mechanism involving Ps for the right side background is the summing of two γ-ray energies where one γ ray goes directly from the annihilation site to the Ge detector. A second γ ray from the same decay, emitted in roughly the opposite direction can Compton scatter in nearby material. If the reemitted γ ray hits the Ge detector, its extra energy will be summed with the first γ ray. The energy dependence for both background processes is smooth enough that a straight, sloped line can adequately fit the data out to 19 keV to the right of the 511-keV peak.

The background on the left side (lower energy) of the 511-keV peak is enhanced by the addition of two new background mechanisms. The first is small-angle Compton scattering of the 511-keV γ rays in the intervening material before getting to the Ge crystal. The second mechanism and the dominant source of left background events involve the three-photon decay of *o*-Ps. The single-photon energy spectrum from three-photon decay is continuous and rises from 0 to 511 keV where there is a sharp cut off [56]. The energy dependence of the two new, nonpeak backgrounds is also sufficiently smooth that a sloped straight line can adequately fit a region 19 keV to the left of the 511-keV peak.

Note in Fig. 3 at 511 keV, where the left and right side backgrounds should exhibit a step function, the backgrounds on the two sides are smoothly connected. The step function in the background has been convolved with the intrinsic resolution of the Ge detector as determined from the ^{106}Ru calibration runs. The 511.86-keV Ru γ-ray line shape, as experimentally measured, is used as the Ge detector resolution function at 511.0 keV.

In preliminary fitting, both the wide and narrow components at 511 keV are represented as Gaussians with adjustable widths and amplitudes and a single centroid. The Gaussian peak shapes are also convolved with the Ge resolution function before fitting. The peak shapes shown in Fig. 3 for the narrow and wide components have been convolved with the Ge detector resolution function. The actual width of the narrow Gaussian alone for the run depicted in Fig. 3 is about 0.5 keV, almost three times narrower than the narrow component shown in Fig. 3.

The final, very small feature in Fig. 3 is a two-photon (2γ) tail appearing at and just above 511 keV. The 2γ tail is due to a summing of energies from two photons emitted in almost the same direction from a single 3γ *o*-Ps decay. If both of the two photons strike the Ge detector, their energies will be summed together. The phase space for such decays is small, but not negligible. To reduce the effect to the size shown in Fig. 3, a 1.6-mm-thick Pb absorber is placed in front of the Ge detector (see Fig. 2). The Pb absorber selectively attenuates the 2γ tail events much more than the 511-keV γ-ray signal events. The unconvolved shape of the 2γ tail is a sharp rise at 511 keV and then a roughly exponential decrease at higher energies. The 2γ tail shown in Fig. 3 has been convolved with the *o*-Ps narrow Gaussian component and the Ge detector resolution.

In this apparatus, the 2γ tail can be readily observed protruding to the right of the 511-keV peak only under special conditions: removing the 1.6-mm Pb shield and turning off the magnetic field. With no perturbed *o*-Ps, turning off the field removes most of the two-photon decay events from the delayed time window, but not all. A much more sensitive study of the 2γ tail was performed in a similar previous experiment [57] with *o*-Ps confined in a MgO-lined, evacuated cavity. The results of the previous tests [57,58], combined with the present $B=0$ observations, lead to the 1.6-mm-thick Pb shield.

The small-angle Compton scattering of 511-keV γ rays penetrating the 1.6 mm of Pb and the vacuum vessel was also studied with the Ge detector. A small-angle scattering of γ rays removes a relatively small fraction of the γ-ray energy. These scattering events result in an increased background to the left of the 511-keV peak. The background to the left of the 511-keV peak originates mostly from single-photon events from 3γ *o*-Ps decay, but small angle scattering is a non-negligible component. The exact ratio of these two processes depends on gas density and composition; typically, scattering is a few percent.

Of the various components discussed, the second wider peak provides the most difficulty for extracting the narrow Gaussian width. Modeling this wider component with a single Gaussian is clearly not correct since it comes from a number of sources. While each of these sources obtains its momentum from a bound electron and is therefore clearly wider than the primary narrow Gaussian, there is no reason to believe that they are identical. This was addressed in our previous work [12] by fitting this component with both a Gaussian and a non-Gaussian shape and comparing the two

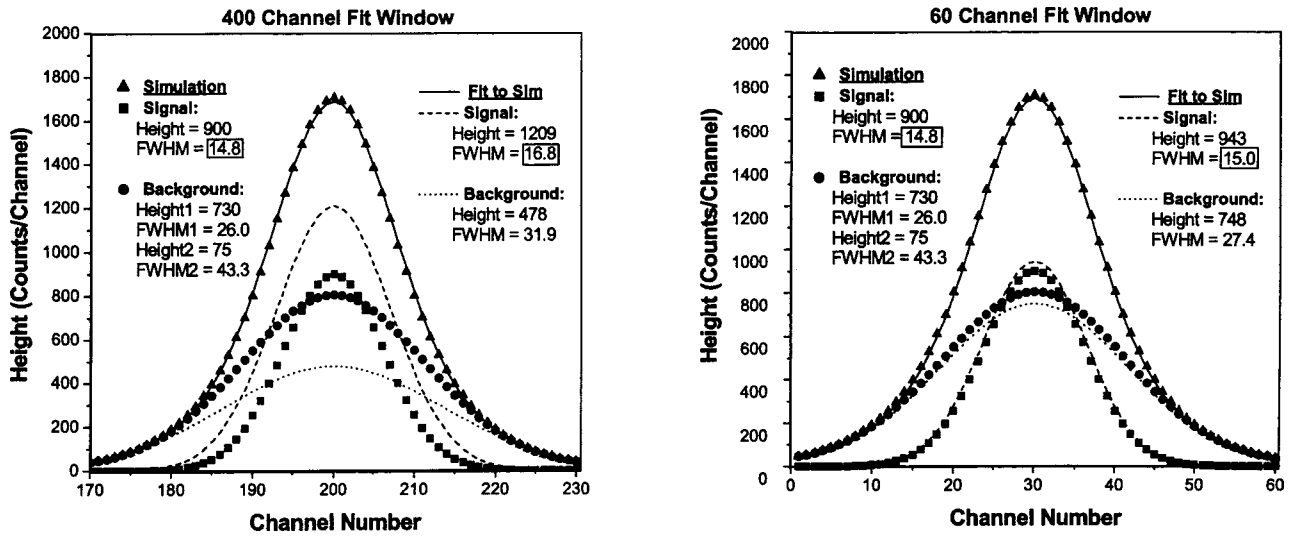

FIG. 4. Effects of fit window. A simulation with two wide Gaussians and one narrow Gaussian is fit with only one wide and one narrow Gaussian. The fit to the simulated data is shown for fit windows of 60 and 400 total channels. Although the overall fit is excellent in both cases, the narrow and wide Gaussians are much more accurate with the 60 channel fit window. In particular, the narrow Gaussian width differs by 2.0 channels for the 400 channel fit and by only 0.2 channels for the 60 channel fit.

results. This rudimentary method was a good test of the sensitivity of the overall fit to changes in the shape of the model. However, it was unable to provide a quantitative measurement of systematic uncertainties introduced by an inaccurate model of the wide peak.

Computer simulations are generated and fit in order to carefully study the systematic effects introduced by the wide peak. A simulated spectrum is generated using three Gaussians, one for the narrow peak and two for the wider peak. This simulated spectrum is fit with only two Gaussians, one for the narrow peak and one for the broader peak. The intent of the simulation is to quantify the effects induced by the second wide Gaussian in the simulation on the overall fit of the spectrum. Figure 4 shows an example of a spectrum generated by the simulation and the fit to that spectrum. For the purposes of this experiment, the only parameter important for determining the Ps energy is the width of the narrow Gaussian. Figure 4 depicts a scenario in which fitting a spectrum with two Gaussians yields statistically good results that are inaccurate in their fit of the narrow peak. Clearly, such effects must be taken into account when fitting actual data. This can be accomplished by varying the window width about the peak that is fit. The systematic effect that arises from an inaccurate model of the wide peak will vary as differing amounts of the wide peak are included in the fit. This is demonstrated in Fig. 4 [19].

Our model of two Gaussians is certainly not a correct representation of the numerous contributions to the wider peak. Generating three Gaussians in the wider component of the simulation was also tested in the above fashion. It was found that this additional degree of freedom did not significantly change the size of effects that could be induced in the fit to the narrow peak. Therefore, only two Gaussians were used to simulate the wide peak.

In order to apply this technique to real spectra, each of the many spectra are fit with varying windows at a single pressure. The results of all the runs for a single pressure are then averaged together to find the average value of the FWHM and height of the two Gaussians for that pressure. The results for each of these four parameters are then plotted versus the width of the fit window and compared with results from fits of a simulation. The input parameters of the simulations are then adjusted until the results of the simulation fits are comparable to the fits of the real data. Limits are assigned to the narrow component by adjusting the narrow component of the simulations until the simulation can no longer be made to match the real data. An example of this for 100 Torr of N_2 can be seen in Fig. 5. The final result for the narrow Gaussian width extracted for a given pressure is then the average of these limits with half of their difference as an estimate of the one standard deviation error bar.

This analysis is an improvement over that presented in our previous paper [12]. In that paper, depending on the gas, data were thrown out at both high and low gas densities when there was difficulty separating the wide and narrow peaks. With the current analysis, this problem was eliminated. Currently, data are eliminated when we are unable to statistically separate the narrow peak from the energy resolution of the HPGe detector. This occurs at the highest gas densities of N_2 and H_2.

As an aside, the two next heaviest noble gases, Kr and Xe, were run on our apparatus, each at a variety of densities. Unfortunately, the analysis specified above was unable to obtain reliable narrow component widths for these gases and therefore no thermalization results can be quoted. One interesting, but crude observation during these runs is that the Ps event rates in our 30 to 50 ns time window for both Kr and Xe did not show the dramatic reduction predicted by the observed dearth [59] of long-lived Ps, i.e., a very small Ps formation fraction.

The fitted result for the width of the narrow Gaussian is used to compute an average rms kinetic energy for *o*-Ps. The

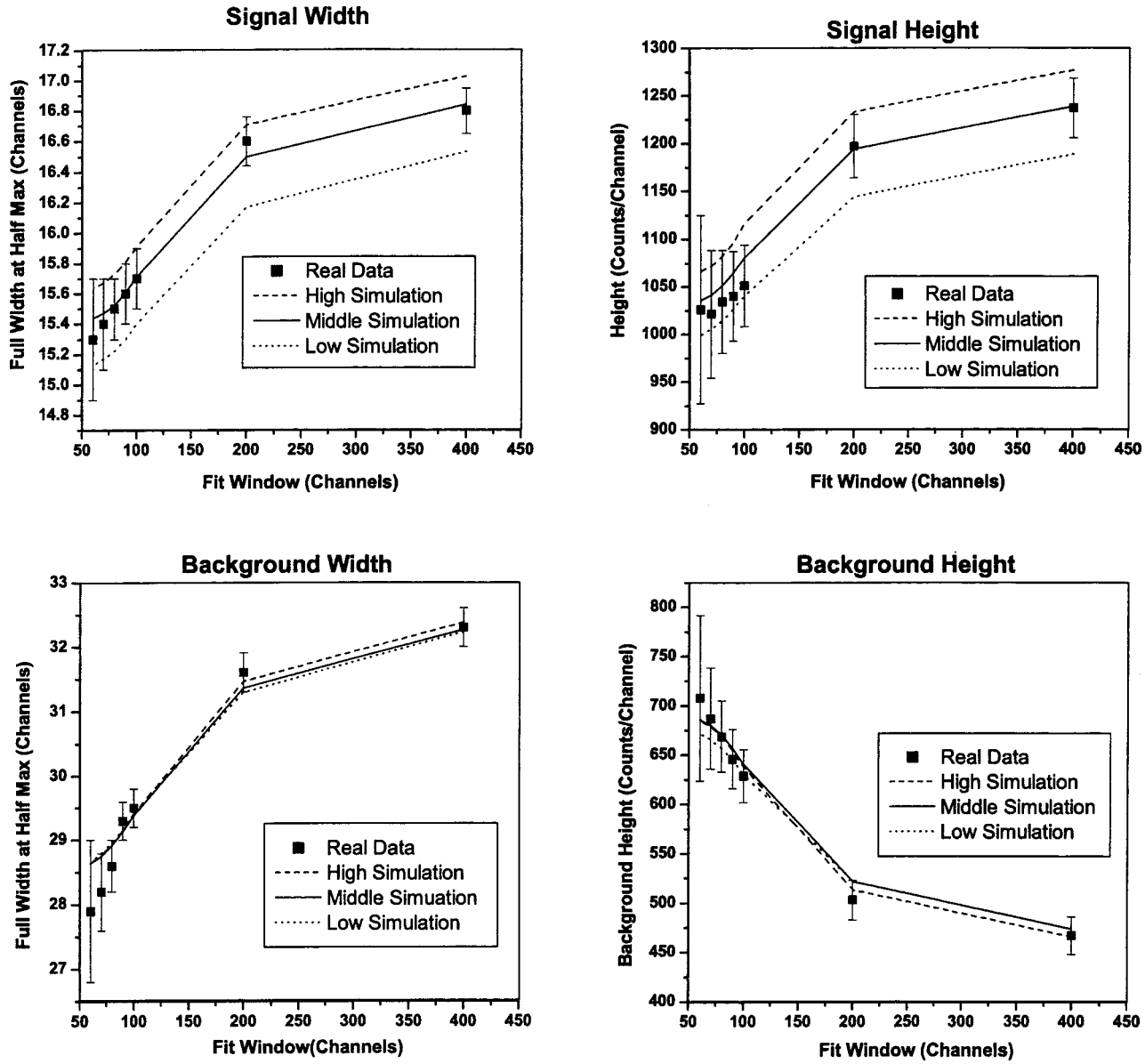

FIG. 5. Determination of the narrow width and associated error bars. The simulations for 200 Torr N_2 are shown. The fits to the width and height of the narrow and wide Gaussians are shown for various fit windows ranging from 60–400 total channels. Simulations are generated and then fit to match the systematic shifts in the fit to each of the four parameters. The dashed line shows the simulations that represent the limits of a good fit to the real data.

o-Ps energy E, in eV, is given by [60,61]

$$E=(1.0288W)^2, \tag{8}$$

expressing the Gaussian width W (FWHM) in keV. This Doppler-broadening formula is derived assuming the thermalizing Ps has a Maxwell-Boltzmann distribution of isotropic velocities. A thermal, isotropic distribution of velocities becomes a Gaussian in the DBS spectrum. It is clear that at the time of formation, the Ps velocities are isotropic, but certainly not a simple thermal distribution at some elevated temperature. The simplest Öre picture [2] of Ps formation predicts an initial energy distribution that is flat from 0 to 6.8 eV. After formation, as the Ps scatters from the gas atoms, the average Ps energy decreases and the distribution approaches a Maxwell-Boltzmann form. This investigation produced no evidence for a nonthermal distribution (non-Gaussian narrow component) even for the spectra taken closest to the formation condition. Unfortunately, the sensitivity to non-thermal distributions is not great due to the underlying wide component in the DBS spectra and a lack of statistics.

To observe the *o*-Ps thermalization process, the average *o*-Ps energy in a typically 30 to 50 ns delayed time window is measured at a given gas density. By either raising or lowering the gas density (time window fixed), a later or earlier part of the thermalization process can be accessed, and the *o*-Ps energy measured. This method of observing the thermalization process makes no assumptions about the functional form of the energy-loss cross section, in contrast to

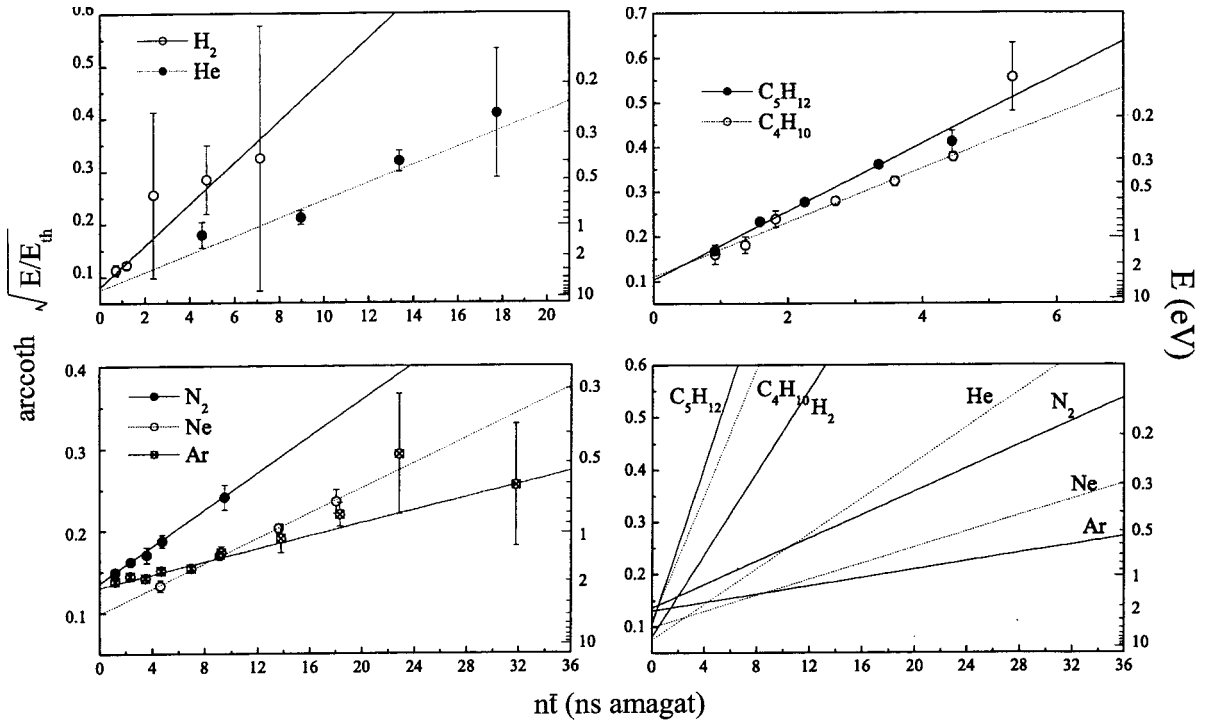

FIG. 6. Fit to Sauder's thermalization model [20]. For seven different gases, the thermalization rate is given by the slope of each line and initial energy can be determined from the zero intercept. The bottom right figure shows only the fits for all of the gases for the sake of comparison. Runs done at 100-Torr pressure appear here at about 4.6 ns amagat.

previous high-resolution ACAR studies of *o*-Ps thermalization in gases [9–11] which do not time select.

The results for *o*-Ps energy versus gas density are analyzed using the classical elastic scattering model proposed by Sauder [20]. A slight modification to Eq. (5) results in a linear equation in density *n*,

$$\operatorname{arccoth}\sqrt{\frac{E}{E_{th}}}=\beta+\Gamma n\bar{t}, \tag{9}$$

identifying t as $\bar{t}$, an average of t over the delayed time window. The averaging for $\bar{t}$ is weighted by the distribution of perturbed *o*-Ps events in the time window. Most of the thermalization data are taken with a 30 to 50 ns time window and $B=2.85$ kG ($\tau_{\mathrm{pert}}=52$ ns), resulting in $\bar{t}=38$ ns. Plotting the *o*-Ps energy according to Eq. (9) versus $n\bar{t}$ will result in a straight line if the classical elastic scattering model adequately describes the actual thermalization process. The slope of the line is the density-normalized rate of *o*-Ps thermalization, Γ. The zero density intercept of the straight line is related to the average *o*-Ps formation energy β [Eq. (3b)].

Remarkably, for all seven gases studied in this investigation, straight lines give reasonable fits to all the data, as shown in Fig. 6. The zero density intercepts for all the gases cluster into a small region corresponding to initial Ps energies of 2 to 7 eV. This is not surprising since the simplest Öre model picture would predict $6.8/2=3.4$ eV as the average initial Ps energy. More surprising, the molecular gases, especially isobutane and neopentane, display quite good linear fits over the energy range investigated. These linear results are difficult to understand since inelastic excitations of the molecules (electronic, vibrational, or rotational) when colliding with *o*-Ps seemingly should introduce some structure in the linear plots. As the *o*-Ps energy becomes lower, fewer inelastic channels are open, slowing the thermalization process. While it is true that there is always a fairly broad distribution of energies present and averaging over this distribution will tend to dilute inelastic structures, the complete absence of structure is still surprising. Certainly for the hydrocarbon molecules and perhaps the diatomic molecules,

TABLE I. Results for Ps thermalization. The table displays $1/\Gamma$, the inverse of the Ps thermalization rate per amagat, i.e., at one atmospheric pressure (STP); E_0, the initial formation energy; ΔE, the range of the measurements; σ_m, the derived elastic scattering cross section. It is assumed that M in Eq. (4) is that of the molecule.

Gas	$1/\Gamma$ (ns amagat)	E_0 (eV)	ΔE (eV)	σ_m (Å^2)
H_2	25 ± 5	$6.0^{+1.6}_{-1.1}$	0.39–3.00	3.3 ± 0.7
He	59 ± 16	7^{+34}_{-4}	0.25–1.20	2.8 ± 0.8
Ne	130 ± 3	$3.92^{+0.15}_{-0.14}$	0.71–2.18	6.40 ± 0.15
Ar	254 ± 38	$2.25^{+0.09}_{-0.08}$	0.47–2.02	6.6 ± 1.0
N_2	90 ± 4	$2.07^{+0.04}_{-0.03}$	0.68–1.73	13.0 ± 0.5
C_4H_{10}	16.6 ± 1.2	$3.1^{+1.0}_{-0.7}$	0.15–1.52	146 ± 11
C_5H_{12}	13.2 ± 0.8	$3.6^{+0.7}_{-0.6}$	0.25–1.39	228 ± 13

the observed thermalization rate should be considered an effective rate for the energy range studied.

In Table I, the results for all seven gases are summarized. The density units for n are amagats, one amagat being the density corresponding to one atmosphere pressure at STP ($n=2.69\times10^{19}/\mathrm{cm}^3$). The reciprocal of the density-normalized thermalization rate, Γ, is the thermalization time at one amagat. The range ΔE in Table I is the energy interval of these thermalization measurements. Note from Eq. (4), Ps thermalization measurements are sensitive to the quantity σ/M for elastic scattering, where M is the mass of the struck atom. For noble gases, M is unambiguous. For molecular gases, however, M might be an atomic mass or the molecular mass or something in between. For the purposes of reporting σ in Table I, the molecular mass is used to facilitate comparison with previous ACAR results.

Before this investigation, the initial energy of the long-lived Ps formed in gases was experimentally inaccessible, but generally believed to be about (6.8/2) eV from the Öre gap argument [2]. The initial energy distribution is almost certainly not Maxwell-Boltzmann, the distribution used for averaging in the Sauder model. In spite of this difference, reasonable estimates of the initial energy can be made from these DBS data.

VI. SYSTEMATIC TESTS OF TIME-RESOLVED DBS IN H_2, N_2, AND NEOPENTANE

An important feature of Sauder's classical model involves the simple scaling of gas density n with t, time since Ps formation. In Eq. (3a), these quantities only appear once and as the simple product (nt). That is, the thermalization of Ps in different densities of the same gas is simply related by a scaling of time. This can be understood physically from the following facts. The progress of the Ps thermalization process depends solely on the number of gas atom collisions experienced by the Ps atom after formation. Since the collision rate is directly proportional to density [Eq. (2)], the thermalization process scales exactly with (nt).

This property of (nt) scaling in the Ps thermalization process is not restricted to just classical scattering. The arguments above are not dependent on elastic scattering or classical scattering. Any mechanism for Ps energy loss in scattering, whether elastic or inelastic, classical or quantum mechanical, must exhibit scaling of the product (nt). This (nt)-scaling principle is used as a basis for several systematic tests of the time-resolved DBS technique.

These systematic tests involve varying the magnetic field and/or the delayed time window. Changing only the magnetic field should, in principle, make no difference to the thermalization measurements. However, the perturbed o-Ps lifetime depends strongly on the B field strength, affecting the statistical efficiency of the DBS technique and the calculation of $\bar{t}$. On the other hand, changing the delayed time window is a direct systematic test of the time-resolved DBS technique and should produce essentially the same results as changing the gas density when $\bar{t}$ is properly evaluated. A variety of test runs are used with H_2, N_2, and neopentane. Higher and lower values for both the time window and the B field are employed. Along with the usual 30 to 50 ns window, a 50 to 80 ns window and a 25 to 40 ns window are also used. Along with the usual $B=2.85$ kG, $B=2.0$ and 3.5 kG are also employed. The results are summarized in Fig. 7. The nonstandard results (i.e., not $B=2.85$ kG and 30 to 50 ns window) have not been subject to the selection procedure. The error bars shown in Fig. 7 are statistical only. The lines are not fits to the data in Fig 7, the lines come from Fig. 6.

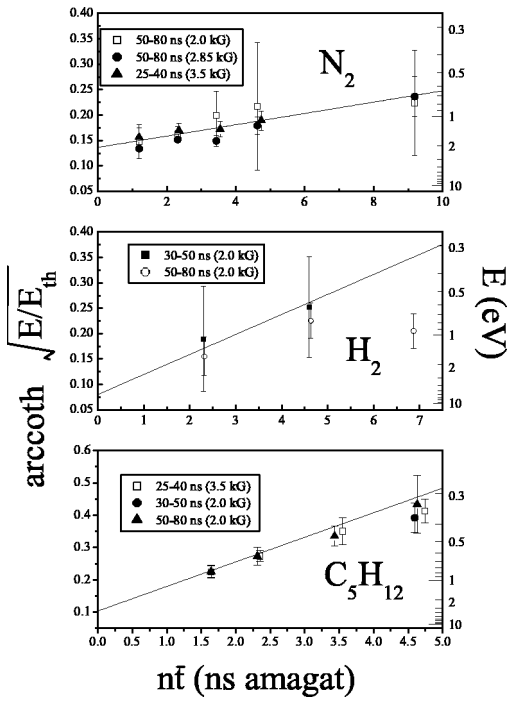

FIG. 7. A summary of the systematic tests performed for various nonstandard time windows and magnetic fields. The lines shown are the best-fit lines for the standard 30–50 ns time window and 2.85-kG magnetic-field strength as shown in Fig. 6 and Table I.

Another possible systematic effect to consider involves the time interval necessary for a beta decay positron to slow down to ≈10 eV and form Ps. Initial timing is derived near the beta source and, in low-density gases, there may be a significant time interval before Ps formation. Unlike Ps, which loses energy very slowly since it is neutral, a charged positron slows down quickly. A conservative estimate indicates that the positrons in this apparatus slow down in less than 1 ns at the lowest densities encountered in these DBS studies. This 1-ns limit on the delay is an order of magnitude smaller than the time resolution of the system. Hence, positron slowing down time is a negligible systematic effect.

VII. DISCUSSION OF RESULTS

Several recurring features are evident in this investigation. Reliable fitting of the narrow o-Ps Doppler component occurs only in a certain restricted Ps energy range for any specific gas. The extreme limits are 0.15 eV (isobutane) to 3 eV (H_2). Measurements at the high energy end of these limits use low gas density runs, which are statistically inhibited for all the gases. At higher gas densities, the slow e^+ properties of the individual gases become important. Unlike most

gases, isobutane and neopentane rapidly annihilate slow e^+, causing their high-density runs (low-energy limits) to be limited by the Ge detector resolution and stability. For the nonhydrocarbons at higher gas densities, slow e^+ contaminate the DBS spectrum with a wide component that increases in amplitude with increasing gas density. The repeatedly observed effect on the fitting routine is to return a narrow component width that is speciously too large, overestimating the Ps energy. The overestimating effect is seen in both the nonhydrocarbon gases and in the systematic tests of the delayed time window. Clearly, an asymmetrical systematic error could be applied to these DBS results to account for the uncertainties introduced by the wide component. We have elected not to apply an asymmetric systematic error bar. The analysis scheme, as depicted in Figs. 4 and 5, cannot also decide the asymmetry in the error bar. The data in Fig. 7, while indicating a possible need for an asymmetric error, cannot quantify the effect. The N_2 data shown in Fig. 7 precisely follow the line from Fig. 6. The neopentane data in Fig. 7 are just beginning to observe the overestimating effect in higher density runs, that is, the data points are starting to fall below the line. The overestimating of the narrow component width is most pronounced in the high density H_2 run, where the point is more than $4\sigma_{stat}$ below the line. Comparison of this point in Fig. 6 indicates why such a large error bar appears in Fig. 6 resulting from the analysis scheme depicted in Figs. 4 and 5. The new analysis scheme has quantified and accounted for the systematic bias introduced by the presence of the wide component in the DBS spectrum. The data presented in Fig. 7 provide an experimental verification of the new analysis scheme and its conservative handling of the systematic effects.

Even with all of the above qualifications, these DBS results often differ significantly from the results obtained from ACAR and, where available, most theory. For N_2, the latest ACAR result is $\sigma_m = 26 \pm 8$ Å^2 compared to $\sigma_m = 13.0 \pm 0.5$ Å^2 determined by this study (Table I), less than a 2σ difference. For H_2, the latest ACAR result is $\sigma_m = 17 \pm 5$ Å^2 [62] compared to 3.3 ± 0.7 Å^2 from this investigation. The older theoretical H_2 calculation [42] is an order of magnitude larger than either experimental result. The recent theory [43] is in good agreement with the present DBS result, perhaps indicating that the ACAR result for the H_2 cross section may be too large.

The theoretical situation with He is much more complex since there are many more calculations as shown in Fig 1. The disagreement between theoretical He calculations is as large as the disagreement between the experimental values. For He, the latest ACAR result is $\sigma_m = 11 \pm 3$ Å^2 [62] compared to 2.8 ± 0.8 Å^2 from this investigation. These two experimental cross sections are shown in Fig. 8 at the average Ps energy of each cross section measurement. Also shown in Fig. 8 are the highest [46] and (absolute) lowest [50] theoretical curves from Fig. 1. An old measurement of the scattering length [63] is also included in Fig. 8. Note that the highest theoretical curve from Fig. 1 has an attached point in Fig. 8. This extra point depicts the momentum-transfer cross section at the center of the energy interval of our measurements, as given in a footnote in Ref. [51]. Despite universal

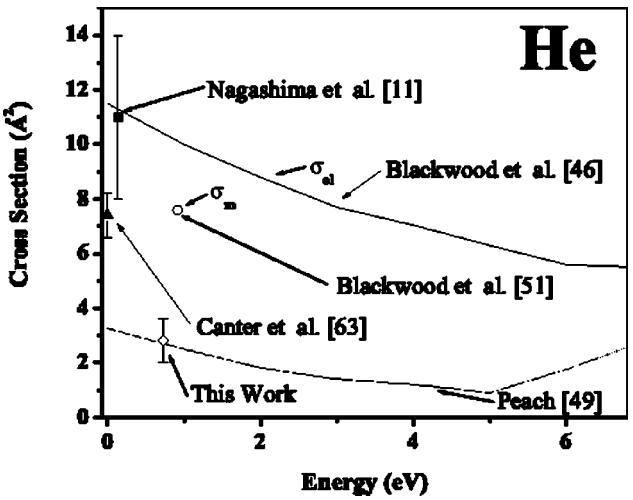

FIG. 8. Comparison of theory and experiment for He scattering. Measurements of the momentum-transfer cross section, σ_m, are plotted at the average Ps energy for each experiment. From Fig. 1, only two elastic scattering calculations are displayed, those with the largest and the smallest cross section. Where available, the theoretical momentum-transfer cross section has been added, in this case, given at just one point, the average energy for our experiment.

expectations that *S*-wave elastic scattering should dominate when Ps is thermalizing in noble gases, a large *P*-wave and higher wave contributions have been found in the latest calculations [51], indicating a difference between σ_{el} and σ_m, the latter being the experimentally measured quantity. Consequently, much more care is needed in comparing experimental cross sections with theoretical calculations. Only in Ref. [51] have appropriate calculations been done to obtain σ_m, incidentally reducing the disagreement between our experimental σ_m for He and the theoretical calculation [46] by almost a factor of 2. It is unknown how much σ_m and σ_{el} differ for the other calculations. But even with the predicted sharply dropping cross sections in Fig. 8, it is unlikely that

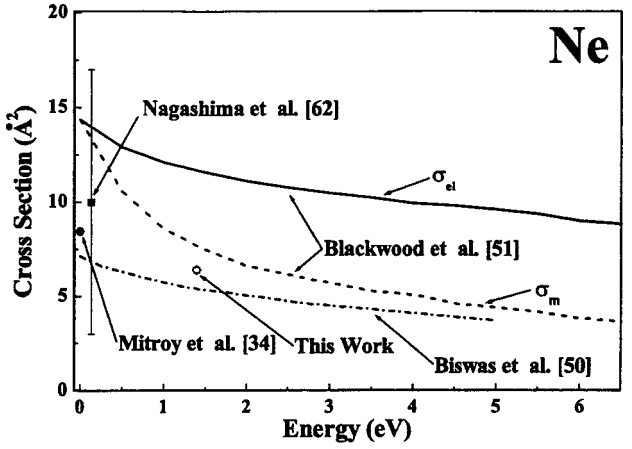

FIG. 9. Comparison of theory and experiment for Ne scattering. Measurements of the momentum-transfer cross section, σ_m, are plotted at the average Ps energy for each experiment. The elastic scattering calculations have also been plotted. Where available, the theoretical momentum-transfer cross-section curve has been added.

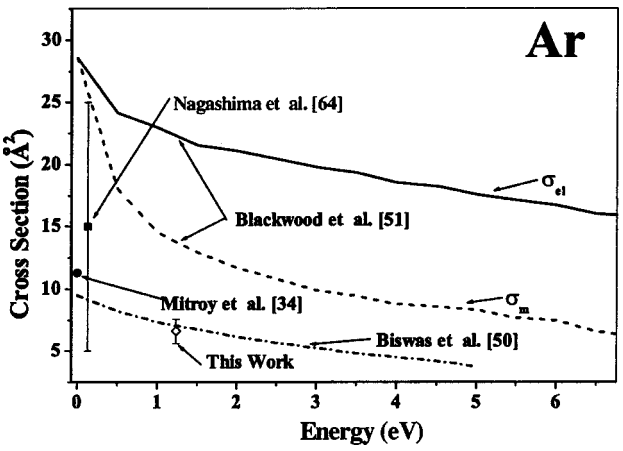

FIG. 10. Comparison of theory and experiment for Ar scattering. Measurements of the momentum-transfer cross section, σ_m, are plotted at the average Ps energy for each experiment. The elastic scattering calculations have also been plotted. Where available, the theoretical momentum-transfer cross-section curve has been added.

the ACAR measurements [62,11] and our DBS measurement can be brought into accord. However, our DBS measurement and the scattering length measurement [63] could be connected by a quickly dropping curve and may not be in disagreement.

The situation with the Ne cross sections is similar to He, including the σ_m problem. The very latest calculations [51] contain substantial P and higher wave contributions leading to a large difference between σ_{el} and σ_m at a few eV, as shown in Fig. 9 with the experimental data for comparison. The ACAR measurement [62] for Ne yields $\sigma_m = 10 \pm 7$ Å^2 and our DBS value is $\sigma_m = 6.40 \pm 0.15$ Å^2, agreement only because of large error bars. The theoretical calculations are quite discrepant. Similarly for Ar, the comparisons are shown in Fig. 10 with the difference between σ_m and σ_{el} shown for Ref. [51]. The experiments are in nominal agreement and theory calculations are discrepant.

To summarize the situation for Ps in noble gases, the experimental Ne and Ar momentum-transfer cross sections are in good agreement for the ACAR and DBS techniques. For He, the ACAR and DBS techniques give apparently inconsistent cross sections even though the measurements are done at slightly different Ps energies. The theoretical situations for He, Ne, and Ar, all feature calculations with differing cross sections, by as much as an order of magnitude. Most of these calculations indicate a decrease in cross section with increasing Ps energy. In an attempt to investigate this feature of the calculations, the Ne and Ar DBS data are fit to a Sauder-like [20] thermalization model but with a v^{-1} dependence for the cross section, instead of a constant cross section [20]. The Ne and Ar DBS data fit this v^{-1} model in a manner just as reasonable and acceptable as the Sauder model shown in Fig. 6. The conclusion is that one cannot discern from these DBS data whether the cross section is constant, Fig. 6, or is sharply decreasing with energy.

The clear difference in both He and H_2 experimental cross-section values between ACAR and DBS may be due to systematic problems in handling the aerogel subtraction for ACAR [10,11,62,64,65]. The ACAR H_2 and He values presented here [11,62] were revised downwards by factors of 3–5 from the upper limits appearing in an earlier report [10]. The revision came about from a different treatment of Ps elastic scattering in the aerogel [64,65]. Clearly, the ACAR results are very sensitive to the treatment of the aerogel thermalization process.

Another systematic problem with the aerogel ACAR technique is the assumption that the *o*-Ps released into the microvoids has the same initial energy distribution with and without gas added to the aerogel. The absorption of the gas onto the walls of the microvoids changes the character of these surfaces. This change can be important since either long-lived Ps is formed on these surfaces or Ps from the bulk must pass through these surfaces to get into the microvoids. If the initial Ps energy distribution is changed by adding a gas, the aerogel subtraction employed in the ACAR studies will lead to erroneous results. Further, there is experimental evidence of this very problem occurring in one aerogel thermalization investigation [61]. Time-resolved DBS studies of aerogel with and without 0.2 atm O_2 give an apparent contradiction, adding gas slows thermalization. Either the initial Ps energy is much higher with gas added or inelastic Ps-surface interactions are much weaker with gas added. Either scenario is systematically awkward for interpreting aerogel ACAR data with and without gas. Admittedly, O_2 gas is probably more reactive with the aerogel microvoid surfaces than some of the other gases studied in Refs. [10,11,62,64,65]. But, all gases, even noble gases, absorb to aerogel, just in differing amounts and probably with different effects on the microvoid *o*-Ps, both in formation and in subsequent wall scatterings. These systematic problems may account for the consistently much larger H_2, N_2, and He cross sections obtained with the aerogel ACAR technique [10,11,62,64,65] compared to the DBS results presented here.

For molecular gases, there is a little theory for H_2, as previously discussed, and none for heavier molecules. The ACAR result for the isobutane cross section is an upper limit of 210 Å^2 [10], compared to (144 ± 19) Å^2 found here with DBS. Is an isobutane molecule actually this large in a classical sense? Simple bond-length arguments would predict a classical size several times smaller than these observations. Perhaps, rovibrational excitations of the isobutane molecule by the colliding *o*-Ps are increasing the apparent molecular size by speeding up the thermalization process with inelastic energy losses. The IR spectra of isobutane and neopentane both have a strong line indicating a vibrational level at 0.17 eV [66], which unfortunately is outside the Ps energy range investigated here for neopentane and just barely inside for isobutane. Other, weaker IR lines [66] indicate that both elastic and inelastic energy-loss processes could be operating in the Ps energy range observed in the DBS thermalization experiment. If inelastic collisions contribute significantly to Ps thermalization, then the straight lines for isobutane and neopentane in Fig. 6 are simply fortuitous and probably due to the broad energy distribution for a thermalizing Ps sample.

The same logic of inelastic, vibrational excitations applied to H_2 and N_2 seems to predict curved lines in Fig. 6. The number of vibrational excitation levels in both molecules is

several per eV [52]. Over the Ps energy range investigated for these two molecules, the number of available inelastic channels changes dramatically. One would expect a larger inelastic cross section at higher Ps energies with more avenues for inelastic energy loss. Elastic scattering calculations for H, H_2, He, Ne, and Ar all have the opposite energy dependence, with cross sections decreasing at higher Ps energies. The straight lines observed for non-noble gases in Fig. 6 could also be due to a near cancellation of inelastic and elastic energy dependencies leaving a roughly constant total cross section.

The contribution from inelastic scattering between ≈ 1 eV Ps and molecular gases is usually assumed to be comparable to inelastic contributions observed in electron scattering [67] and scattering with regular atoms and molecules. Yet, the case of Ps scattering is quite different and unique because of the combination of small mass and neutral charge. The interaction of a Ps atom with a gas molecule is, by necessity, short ranged and, since Ps moves so fast, of short-time duration. The usual view of Ps scattering from the whole molecule [10] may be incorrect.

Consider the relative thermalization rates of He, Ne, and N_2 as shown as their slopes in Fig. 6, lower right. Note the slope of the N_2 line falls between the He ($M=4$) and the Ne ($M=20$) lines. This fact could indicate that Ps scatters from only a single N atom ($M=14$), not the entire molecule. In this interpretation of M in elastic scattering, the N_2 and H_2 cross sections presented in Table I would need to be reduced by a factor of 2 and expressed as N and H cross sections of 6.5 $Å^2$ and 1.65 $Å^2$, respectively.

Using this same scattering picture, the large saturated hydrocarbon molecules used in these studies may appear to Ps as an isolated ''clump'' of several H atoms. For elastic scattering, the M used in Eq. (4) could be as small as a few compared to 58 and 72 for isobutane and neopentane molecular masses. The cross sections appearing in Table I for these molecules would be substantially reduced with this new interpretation. Also, the excitation of certain vibrational and rotational modes would be forbidden in this alternate view of Ps scattering with molecules. For both isobutane and neopentane, vibrational excitations involving only C-H bonds all have energies above 0.17 eV. Conversely, vibrational excitations involving C-C bonds, deep inside the molecule, are all below 0.17 eV [66]. One might expect a dramatic effect on Ps thermalization when crossing this 0.17-eV threshold. Unfortunately, 0.17 eV is near the bottom of the range of the present measurements (see Table I and Fig. 6), but a second-generation thermalization apparatus could easily scan through this energy threshold and search for a reduced thermalization rate at low energy. Until such a test, the correct picture of ≈ 1-eV Ps interacting with molecules will remain a mystery.

VIII. CONCLUSIONS

We have demonstrated that time-resolved Doppler-broadening measurements are a simple, yet powerful technique for observing the formation and thermalization of Ps in gases. Unlike the previous ACAR studies of Ps thermalization, no specific model of Ps energy loss need be assumed. It turns out that a classical elastic-scattering model adequately fits the data for all seven gases studied here. When comparisons can be made, the energy-loss cross sections that are obtained from the fits are often significantly smaller than the ACAR results and most theoretical calculations. A limited Ps energy range from at best 0.15 to 3.0 eV is investigated in the present study. Future studies could expand the Ps energy range and improve the accuracy. An estimate of the initial formation energy of Ps is obtained by extrapolation of the measurements. The initial Ps energies, when accurately obtained, cluster between 2 and 4 eV, as expected from a simple Öre model of Ps formation.

The reliability of the DBS technique has been extensively tested in three of the gases and systematic errors are included in the final results for cross sections and formation energies. The agreement with ACAR experiments is still not good. The treatment of the thermalizing effect of aerogel is critical in interpreting ACAR data. A subtraction of aerogel ACAR with and without added gas assumes no change in Ps emitted from the aerogel grains. Errors could arise in the complex treatment and reduction of ACAR data to obtain cross sections. In comparison, our DBS technique is straightforward and has inherently a better signal-to-noise ratio in the raw data due to time selection. While the ACAR technique has inherently much better instumental momentum resolution compared to DBS, source inefficiencies and uncertainties in the interpretation of ACAR spectra may be causing misestimates of cross sections.

The theoretical progress on Ps gas scattering calculations is not as quick as Massey and Mohr [1] expected, but improving and expanding rapidly. Published calculations of relevance to the Ps thermalization problem are, except for He, sparse and often contradictory. The disagreement between these DBS results and ACAR measurements for He has recently interested theorists and the literature is now expanding rapidly on this difficult scattering problem.

It appears from these DBS results that Ps-gas cross sections are significantly smaller than previously believed. This implies that thermalization times are actually much longer than previously thought. The ramifications of slow Ps thermalization in gases could be substantial in experiments measuring Ps lifetimes in low-density gases. The appearance of Ps thermalization effects in lifetime spectra is characterized by a lifetime that apparently changes as the Ps gets older. Such effects have been observed in high-precision, decay rate (lifetime) studies [14–16]. Understanding these decay rate effects was the original motivation for beginning the DBS investigation and has led to an ongoing reinvestigation of thermalization and quenching issues in decay rate experiments using gases [17]. A small correction to existing gas decay rate results will be published in a forthcoming paper [18].

A replacement gas chamber has been designed for the existing electromagnet and single Ge detector. This revised design is optimized in the sense of (1) greatly increased statistical efficiency, (2) improved signal-to-noise ratio, where the noise here is due to accidental, random coincidences, and (3) increased resolution stability. With the addition of this

gas chamber and upgrading of the data-acquisition electronics, an order of magnitude reduction in cross-section error bars may be possible. The systematic effects of the broad DBS component must also be understood better to extend the present measurements. Access to more thermalization data would greatly aid in the quantitative understanding of the broad DBS component. Externally derived DBS data [68–70] can also, in some instances, be used to specify the form of the broad DBS component observed in our spectra. The possibility of using mixtures of gases to suppress the broad component needs to be investigated as well. In short, the future prospects are excellent for more DBS measurements of Ps thermalizing in various gases.

The hydrocarbon gases studied here, isobutane and neopentane, are noted for rapid quenching of slow positrons. These gases have excellent prospects for expanding the energy range of the Ps thermalization measurements down to thermal. At present, Ge detector resolution stability limits the lowest Ps energies that can be investigated. The resolution stability issue is simply a hardware problem with our data-acquisition system and can be straightforwardly minimized [53].

Other saturated hydrocarbon gases, e.g., methane, ethane, etc., may also be interesting in Ps thermalization studies, but they do not quench slow positrons as readily as isobutane and neopentane. The almost spherical structure of these latter two hydrocarbons may be a special asset in quenching slow positrons. Further, the pick-off quenching of thermalized *o*-Ps is smaller in isobutane and neopentane compared to methane and ethane. There is no clear understanding of the Ps interaction, at 1 eV or thermalized, with these large, complex hydrocarbon molecules. One possible experiment would compare Ps thermalization data in normal neopentane and fully deuterated neopentane. The molecular mass difference (72 versus 84) is small compared to a possible factor of 2 change in mass from which Ps scatters. Such a change clearly could affect elastic scattering and also vibrational excitations [66].

Using electrons or photons as a scattering probe of large hydrocarbon molecules results in a rich spectrum of inelastic excitations: rotational, vibrational, and electronic degrees of freedom are readily accessed for all types of bonds. The present evidence from Ps thermalization is bland in comparison; no inelastic structure is evident for isobutane or neopentane. An improvement in the accuracy of the energy measurements is desirable and may be necessary to resolve elastic and inelastic contributions to the energy loss in Ps thermalization; the same applies to extending the range of the Ps energy measurements.

A second-generation thermalization apparatus could address the issue of inelastic collisions in many possible molecular gases. It could also improve the accuracy of elastic cross sections and the search for their energy dependence in noble gases. The ability to compare experiment with theoretical calculations will expand in future years both for noble and molecular gases, hopefully, leading to the correct view of Ps thermalizing in gases.

ACKNOWLEDGMENTS

We acknowledge useful discussions with T. Chang, P. G. Coleman, R. S. Conti, R. J. Drachman, G. W. Ford, T. Hyodo, K. Iwata, G. Laricchia, R. R. Lewis, R. S. Raymond, C. M. Surko, and J. C. Zorn. We thank P. K. Biswas, H. R. J. Walters, and G. Peach for communications on unpublished calculations. We also thank R. K. Bithell for help in this experiment and A. F. Yee for the use of the Ge detector. This research was supported by NSF Grant No. PHY-9731861 and the University of Michigan.

[1] H.S.W. Massey and C.B.O. Mohr, Proc. Phys. Soc., London, Sect. A **67**, 695 (1954).
[2] A. Öre, *Naturvidenskap Rikke No. 9* (University of Bergen, Arbok, 1949).
[3] R.J. Drachman, *Atomic Physics with Positrons* (Plenum, New York, 1987), p. 203.
[4] N. Zafar, G. Laricchia, M. Charlton, and A.J. Garner, Phys. Rev. Lett. **76**, 1595 (1996).
[5] A.J. Garner, A. Özen, and G. Laricchia, J. Phys. B **33**, 1149 (2000).
[6] A.J. Garner, G. Laricchia, and A. Özen, J. Phys. B **29**, 5961 (1996).
[7] A.J. Garner, A. Özen, and G. Laricchia, Nucl. Instrum. Methods Phys. Res. B **143**, 155 (1998).
[8] S. Takada, T. Iwata, K. Kawashima, H. Saito, Y. Nagashima, and T. Hyodo, Radiat. Phys. Chem. **58**, 781 (2000).
[9] P.G. Coleman, S. Rayner, F.M. Jacobsen, M. Charlton, and R.N. West, J. Phys. B **27**, 981 (1994).
[10] Y. Nagashima *et al.*, Phys. Rev. A **52**, 258 (1995).
[11] Y. Nagashima, T. Hyodo, K. Fujiwara, and A. Ichimura, J. Phys. B **31**, 329 (1998).
[12] M. Skalsey, J.J. Engbrecht, R.K. Bithell, R.S. Vallery, and D.W. Gidley, Phys. Rev. Lett. **80**, 3727 (1998).
[13] A. Rich, Rev. Mod. Phys. **53**, 127 (1981).
[14] C.I. Westbrook, D.W. Gidley, R.S. Conti, and A. Rich, Phys. Rev. A **40**, 5489 (1989).
[15] A.H. Al-Ramadhan and D.W. Gidley, Phys. Rev. Lett. **72**, 1632 (1994).
[16] C.I. Westbrook, D.W. Gidley, R.S. Conti, and A. Rich, Phys. Rev. Lett. **58**, 1328 (1987).
[17] R.S. Vallery, A.E. Leanhardt, M. Skalsey, and D.W. Gidley, J. Phys. B **33**, 1047 (2000).
[18] D.W. Gidley, Bull. Am. Phys. Soc. **43**, 1072 (1998).
[19] C.M. Nakamura, J.J. Engbrecht, M. Skalsey, and D.W. Gidley, Bull. Am. Phys. Soc. **46**, 59 (2001).
[20] W.C. Sauder, J. Res. Natl. Bur. Stand., Sect. A **72**, 91 (1968).
[21] E.W. McDaniel, J.B.A. Mitchell, and M.E. Rudd, *Atomic Collisions–Heavy Particle Projectiles* (Wiley, New York, 1993), p. 10.
[22] M.T. McAlinden, F.G.R.S. MacDonald, and H.R.J. Walters, Can. J. Phys. **74**, 434 (1996).
[23] P.A. Fraser, Proc. Phys. Soc. London **78**, 329 (1961).

[24] S. Hara and P.A. Fraser, J. Phys. B **8**, L427 (1975).
[25] H. Ray and A.S. Ghosh, J. Phys. B **29**, 5505 (1996).
[26] H. Ray and A.S. Ghosh, J. Phys. B **30**, 3745 (1997).
[27] P.K. Sinha, P. Chaudhury, and A.S. Ghosh, J. Phys. B **30**, 4643 (1997).
[28] P.K. Biswas and S.K. Adhikari, J. Phys. B **31**, 3147 (1998).
[29] C.P. Campbell, M.T. McAlinden, F.G.R.S. MacDonald, and H.R.J. Walters, Phys. Rev. Lett. **80**, 5097 (1998).
[30] B.A.P. Page, J. Phys. B **9**, 1111 (1976).
[31] R.J. Drachman and S.K. Houston, Phys. Rev. A **12**, 885 (1975).
[32] R.J. Drachman and S.K. Houston, Phys. Rev. A **14**, 894 (1976).
[33] I.A. Ivanov, J. Mitroy, and K. Varga, Phys. Rev. Lett. **87**, 063201 (2001).
[34] J. Mitroy and I.A. Ivanov, Phys. Rev. A **65**, 012509 (2001).
[35] S.K. Adhikari and P. Mandal, J. Phys. B **34**, L187 (2001).
[36] H. Ray and A.S. Ghosh, J. Phys. B **31**, 4427 (1998).
[37] S.K. Adhikari and P.K. Biswas, Phys. Rev. A **59**, 2058 (1999).
[38] P.K. Sinha, A. Basu, and A.S. Ghosh, J. Phys. B **33**, 2579 (2000).
[39] S.K. Adhikari, Phys. Rev. A **63**, 054502 (2001).
[40] P.K. Biswas, J. Phys. B **34**, 4831 (2001).
[41] S. Zhou, W.E. Kauppila, C.K. Kwan, and T.S. Stein, Phys. Rev. Lett. **72**, 1443 (1994).
[42] M. Comi, G.M. Prosperi, and A. Zecca, Phys. Lett. **93A**, 289 (1983).
[43] P.K. Biswas and S.K. Adhikari, J. Phys. B **31**, L737 (1998).
[44] P.K. Biswas and S.K. Adhikari, J. Phys. B **33**, 1575 (2000).
[45] R.J. Drachman and S.K. Houston, J. Phys. B **3**, 1657 (1970).
[46] J.E. Blackwood, C.P. Campbell, M.T. McAlinden, and H.R.J. Walters, Phys. Rev. A **60**, 4454 (1999).
[47] A.S. Ghosh, A. Basu, T. Mukherjee, and P.K. Sinha, Phys. Rev. A **63**, 042706 (2001).
[48] A. Basu, P.K. Sinha, and A.S. Ghosh, Phys. Rev. A **63**, 052503 (2001).
[49] G. Peach, *Positron Spectroscopy of Solids*, edited by A. Dupasquier and A.P. Mills, Jr. (IOP, Amsterdam, 1995), p. 401, cited by G. Laricchia.
[50] P.K. Biswas and S.K. Adhikari, Chem. Phys. Lett. **317**, 129 (2000).
[51] J.E. Blackwood, M.T. McAlinden, and H.R.J. Walters, J. Phys. B **35**, 2661 (2002).
[52] G. Herzberg, *Spectra of Diatomic Molecules*, 2nd ed. (D. van Nostrand, Princeton, NJ, 1950).
[53] T. Chang, M. Xu, and X. Zeng, Phys. Lett. A **126**, 189 (1987).
[54] G. Gerber, D. Newman, A. Rich, and E. Sweetman, Phys. Rev. D **15**, 1189 (1977).
[55] T.C. Griffith, *Advances in Atomic and Molecular Physics* (Academic, New York, 1979), Vol. 15, p. 135.
[56] T. Chang, H. Tang, and Y. Li, Phys. Lett. **157B**, 357 (1985).
[57] D.W. Gidley, J.S. Nico, and M. Skalsey, Phys. Rev. Lett. **66**, 1302 (1991).
[58] S. Asai, S. Orito, T. Sanuki, M. Yasuda, and T. Yokio, Phys. Rev. Lett. **66**, 1298 (1991).
[59] G.L. Wright, M. Charlton, T.C. Griffith, and G.R. Heyland, J. Phys. B **18**, 4327 (1985).
[60] The disagreement over this formula cited in Ref. [12], different from Ref. [53], has been resolved. See Ref. [61].
[61] T. Chang, *Positron Annihilation, ICPA-8* (World Scientific, Singapore, 1989), p. 150.
[62] Y. Nagashima, F. Saito, N. Shinohara, and T. Hyodo, *New Directions in Antimatter Chemistry and Physics* (Kluwer, Dordrecht, 2001), p. 291.
[63] K.F. Canter, J.D. McNutt, and L.O. Roellig, Phys. Rev. A **12**, 375 (1978).
[64] Y. Nagashima, T. Hyodo, K. Fujiwara, and A. Ichimura, in *The Physics of Electronic and Atomic Collisions*, edited by L.J. Dube, B.A. Mitchell, W. McConkey, and C.E. Brion, AIP Conf. Proc. No. 360 (AIP, New York, 1996).
[65] F. Saito, N. Zafar, Y. Nagashima, and T. Hyodo, in *The Physics of Electronic and Atomic Collisions* (Ref. [64]).
[66] L.M. Sverdlov, M.A. Kouner, and E.P. Krainov, *Vibrational Spectra of Polyatomic Molecules* (Wiley, New York, 1974), translation by IPST Staff.
[67] D.E. Golden, N.F. Lane, A. Temkin, and E. Gerjouy, Rev. Mod. Phys. **43**, 642 (1971).
[68] K. Iwata, R.G. Greaves, and C.M. Surko, Phys. Rev. A **55**, 3586 (1997).
[69] P. Van Reeth, J.W. Humberston, K. Iwata, R.G. Greaves, and C.M. Surko, J. Phys. B **29**, L465 (1996).
[70] S.J. Gilbert, R.G. Greaves, and C.M. Surko, Phys. Rev. Lett. **82**, 5032 (1999).